An Evaluation of Heat Partition in High Speed Turning of AISI/SAE 4140 Steel with Uncoated and TiN Coated Tools

An evaluation of heat partition in the high-speed turning of AISI/SAE 4140 steel with uncoated and TiN-coated tools

F Akbar*, P T Mativenga, and **M A Sheikh**
School of Mechanical, Aerospace, and Civil Engineering, The University of Manchester, Manchester, UK

Abstract: In manufacturing by machining, thermal loads on cutting tools can have a major influence on tool wear and hence process cost, especially at higher cutting speeds. An investigation has been undertaken to determine heat partition into the cutting tool for high-speed machining of AISI/SAE 4140 high-strength alloy steel with uncoated and TiN-coated tools. The cutting tests have been performed at cutting speeds ranging between 100 and 880 m/min with a feed rate of 0.1 mm/rev and a constant depth of cut of 2.5 mm. Cutting temperatures are measured experimentally using an infrared thermal imaging camera. The sticking and sliding regions are investigated from an examination of the tool–chip contact region using a scanning electron microscope (SEM). In addition, non-uniform heat intensity is modelled according to the contact phenomena. In this work, evaluation of the fraction of heat flowing into the cutting tool is carried out by iteratively reducing the available heat flux until the finite element method (FEM) temperatures are simultaneously matched at multiple points with the experimentally measured temperatures. This paper elucidates on the differences in thermal shielding for uncoated and TiN-coated tools. It is found that heat partition into the cutting tool decreases from a fraction of 0.41 to 0.17 for conventional cutting speeds and increases from 0.19 to 0.24 for high-speed machining when using uncoated carbide cutting tools. On the other hand, with TiN-coated tools, heat partition varies from 0.35 down to 0.095 for the whole range of cutting speeds. These results clearly show that the use of TiN-coated tools generally reduces heat partition into the cutting tool, but does so more significantly in high-speed machining (HSM) as compared with conventional machining speeds. The driver behind this study on heat partition in machining with TiN coatings is the design of coatings with enhanced thermal shielding properties.

Keywords: high-speed machining (HSM), contact phenomena, TiN-coated tools, heat partition, finite element method (FEM)

1 INTRODUCTION

High-speed machining (HSM) at significantly increased cutting speeds and feed rates can lead to a significant reduction in the machining time. Therefore, high-speed machining is now recognized as one of the key manufacturing technologies for higher productivity. Key advantages of high-speed machining have been reported as high material removal rates, low cutting forces, the reduction in lead times, and improvement in part precision and surface finish [1]. The distinction between conventional and high-speed machining is based on the workpiece material being machined, the type of cutting operation, and the cutting tool used [2].

Dry HSM demands specially engineered cutting tool materials with extreme hot hardness and improved fracture toughness, as well as resistance to abrasion, thermal shock, adhesion, and diffusion. Among the coatings available in the market, titanium-based thin films have found the widest acceptance. They

*Corresponding author: School of Mechanical, Aerospace, and Civil Engineering, University of Manchester, Sackville Street Building, Manchester M60 1QD, UK. email: faraz.akbar@ postgrad.manchester.ac.uk

tend to improve the wear resistance in many cutting applications [3, 4], by reducing friction, adhesion, and diffusion, and by relieving thermal and mechanical stresses on the substrate. Furthermore, physical vapour deposition (PVD) based TiN coatings are widely used to improve the tribological and mechanical properties of the cutting tool [5, 6].

It is now widely accepted that machining at higher cutting speeds leads to higher tool–chip interface temperatures. The temperature at the tool–chip interface and the heat transferred from this zone are crucial in determining tool wear, tool life, and surface integrity. These influences, which are predominant in dry machining at high speeds, are also extremely important for economical and ecological reasons. While heat generation depends mainly on process parameters and the machinability of the work material, the thermophysical properties of the cutting tool material are important factors in the distribution of temperature fields and heat dissipation [7]. Determination of the maximum temperature and temperature distribution along the rake face of the cutting tool is of particular interest because of their controlling influence on tool performance and tool life, as well as the quality of the machined part [8, 9].

The main regions where heat is generated during the orthogonal cutting process are shown in Fig. 1. First, heat is generated in the primary deformation zone owing to plastic work done at the shear plane. Second, heat is generated in the secondary deformation zone owing to work done in deforming the chip and in overcoming sliding friction at the tool–chip interface zone. Finally, heat is generated in the tertiary deformation zone, i.e. at the tool–workpiece interface, owing to work done to overcome friction that occurs at the rubbing contact between the tool flank face and the newly machined surface of the workpiece. The fraction of heat that flows into the cutting tool, which is stationary relative to the heat source, is based on determination of the heat partition coefficient, R_T, which defines the percentage of heat entering the cutting tool (Fig. 1). The fraction $R_{ch} = 1 - R_T$ defines the heat energy going into the moving chip.

In modelling the effect of the secondary heat source, the heat partition approach is commonly used by considering the tool–chip contact pair. To this end, Blok's heat partition principle [10] has been widely used in the analytical investigation of temperatures generated in metal cutting. Blok's principle models the two bodies in relative motion: one stationary, and the other moving with a relative velocity. Hence, it can be employed to solve the problem of heat partition at the tool–chip interface. Chao and Trigger [11] used Blok's partition principle, assuming a uniform heat partition ratio along the tool–chip

contact length, but failed to achieve an interface temperature rise on the chip in agreement with that on the tool. Later on, Chao and Trigger [12] assumed that the heat intensities along the tool–chip and tool–workpiece interfaces were uniform. Komanduri and Hou [13] furthered the functional analysis approach based on the idea of Chao and Trigger [11]. These studies [12, 13] adopted the concept of a uniform heat intensity along the tool–chip interface. However, it can be argued that, because of the presence of plastic and elastic zones along the contact length, the secondary heat source cannot simply be assumed to be uniform. Huang and Liang [14] used a non-uniform heat intensity along the tool–chip interface in their model and determined heat partition by using the lengths of sticking and sliding zones from other studies. Recently, Karpat and Özel [15, 16] determined heat partition on the basis of a non-uniform heat intensity and calculated the actual lengths of sticking and sliding zones empirically for a carbide tool. Until now, there has been no documented model that considers non-uniform distribution of heat intensity coupled with an experimental quantitative determination of sticking and sliding zones along the tool–chip interface for TiN-coated tools and cutting speeds ranging from conventional to HSM.

Moriwaki et al. [17] reported that half of the heat generated by the friction between the tool and workpiece is supplied to the workpiece and the other half to the tool when machining annealed oxygen-free copper (99.99 per cent) with single-crystal diamond and high-speed steel at cutting speeds of 138 and 276 m/min. Takeuchi et al. [18] has reported that 10 to 30 per cent of the total heat generated enters the tool. They applied this assumption in the machining of carbon steel (C = 0.55 per cent) using P15 carbide tooling at a cutting speed of 100 m/min. According to Wright et al. [19], 80–90 per cent of heat generated at the rake face flows into the chip when machining annealed low-carbon iron with M34 high-speed steel at cutting speeds ranging from 10 to 175 m/min. Lo Casto et al. [20] reported that between 56 and 24 per cent of heat was transmitted into the tool when machining AISI 1040 with a P10 sintered carbide insert at cutting speeds of 99–240 m/min. Grzesik and Nieslony [21] estimated that the fraction of heat going into the tool varied from 35 to 20 per cent when using multilayer coated tools, but changed from 50 to 40 per cent for uncoated carbide tools in the range of cutting speeds of 50–210 m/min for the workpiece material AISI 1045. According to Loewen and Shaw [22], heat transmitted into the tool varies between 40 and 20 per cent when machining AISI/SAE B1113 free-cutting steel with a K2S carbide tool at cutting speeds of 30–182 m/min.
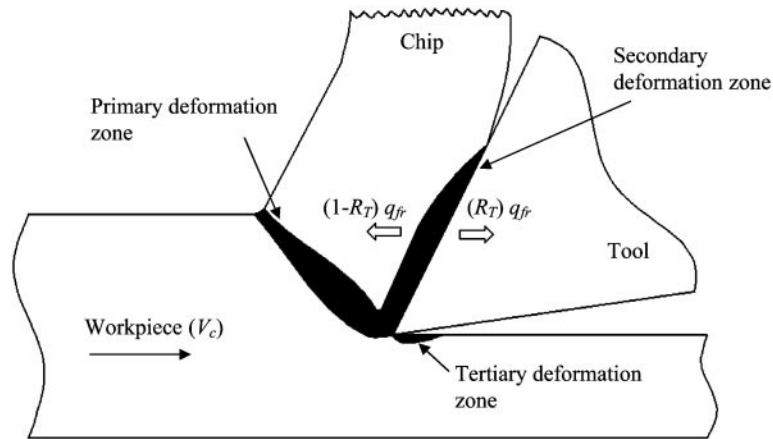
Fig. 1 Illustration of heat generation zones in orthogonal metal cutting

Abukhshim *et al.* [23] evaluated the heat partition coefficient for the tool in the machining of AISI/SAE 4140 steel using P20 carbide tools to vary between 50 and 15 per cent in conventional machining at cutting speeds of 200–600 m/min. There is very limited published work that reports numerical values for heat partition considering workpiece and cutting tool combinations. Most studies, except that by Abukhshim *et al.* [23], have only covered conventional cutting speeds. It is important, however, to establish similar reference values for heat partition over a wider range of cutting speeds including HSM.

This paper presents a combination of experimental and finite element modelling approaches to predicting heat partition in the secondary deformation zone. One novelty of the approach is the development of a technique that takes into account non-uniform heat intensity applied on the basis of a quantitative determination of sticking and sliding zones along the tool–chip interface. In general, the methodology to estimate heat partition into the cutting tool utilizes the tool–chip contact area, the velocity of the chip, the sticking and sliding lengths, the thermophysical properties of the tool, the shim seat and tool holder materials, and realistic and where appropriate non-uniform heat intensity.

1.1 Estimation of non-uniform heat intensity along the tool–chip interface

In machining, the contact phenomena can be characterized by sticking and sliding. This distinction is highly dependent on the tool and workpiece materials, as well as on the cutting conditions. In the sticking zone, the shear stress, τ_{sh}, can be assumed to be constant along the entire sticking (seizure) contact length up to $x = l_{st}$, where x is the distance from the cutting tool edge. In the sliding zone, this shear stress reduces to zero at the point at which the chip departs from the tool rake face. According to Wright *et al.*

[19], the shear stress in the sticking region, τ_{sh}, can be computed from the equation

$$\tau_{sh} = \frac{F_{fr}}{a_p(l_{st} + 0.5\, l_{sl})} \tag{1}$$

where l_{st} is the sticking length of the tool–chip contact zone, l_{sl} is the sliding length of the tool–chip contact zone, a_p is the depth of cut, and F_{fr} is the frictional force which can be calculated from the equation

$$F_{fr} = F_c \sin \gamma + F_f \cos \gamma \tag{2}$$

where F_c is the cutting force, F_f is the feed force, and γ is the rake angle. In this study, the heat intensity $q_{fr}(x)$ along the sticking zone is defined as $\tau_{sh}\, V_{ch}$ ($x \leqslant l_{st}$) which then linearly decreases to zero along the sliding contact zone ($l_{st} < x \leqslant l_{ch}$), as shown in Fig. 2. This heat generation model is used in the present study for thermal modelling of the tool–chip interface. It follows the work of Tay *et al.* [24] and Wright *et al.* [19] who also treated the heat distribution in the sliding region as linear. Recently, Huang and Liang [14] used a similar methodology to evaluate the non-uniform heat intensity but adopted the sticking and sliding length values from other studies. An important input variable, which is used in evaluating the heat intensity at the tool–chip interface, is the chip velocity, V_{ch}. This can be computed from the equation

$$V_{ch} = \frac{V_c}{\lambda_h} \tag{3}$$

where V_c is the cutting speed and λ_h is the chip compression ratio which is defined as

$$\lambda_h = \frac{t_{ch}}{t} \tag{4}$$

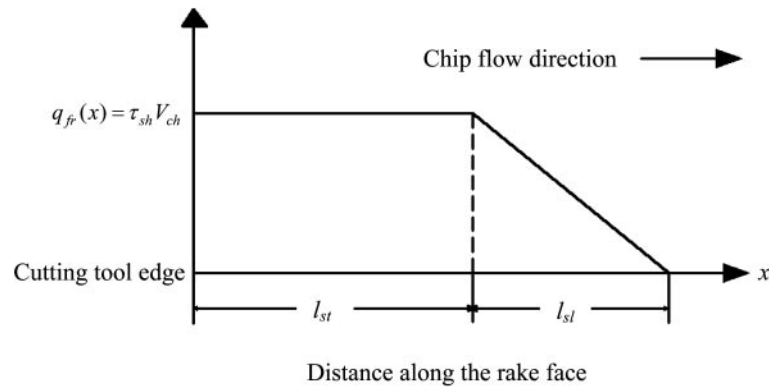where t_{ch} is the actual chip thickness and t is the undeformed chip thickness.

Fig. 2 Non-uniform heat intensity model along the rake face of the cutting tool according to Wright *et al.* [19] and Tay *et al.* [24]

2 EXPERIMENTAL INVESTIGATIONS

2.1 Experimental details

The cutting tests were performed on a Dean Smith & Grace lathe machine. A Kistler cutting force dynamometer model 9121 was used to measure the cutting forces. Tungsten-based uncoated cemented carbide and PVD TiN-coated tools with geometries designated as TCMW 16T304 (ISO specification) (triangular shape insert with 0.4 mm nose radius, 3.97 mm thickness, and 7° clearance angle) were used. The tool holder used was Sandvik STGCR/L 2020K 16 (ISO specification).

A pre-bored workpiece of AISI/SAE 4140 high-tensile alloy steel with an external diameter of 200 mm and 2.5 mm tube thickness was used in the cutting tests. AISI/SAE 4140 was chosen, as it has many diverse applications in the manufacture of automobile components such as crankshafts, piston rods, steering components, axles, gears, and high-resistance screws. Experimental conditions were similar for both cutting tool materials. The cutting tests were performed at eight different cutting speeds of 100, 197, 314, 395, 565, 628, 785, and 880 m/min. These cutting speeds were set by the available rotational speed on the conventional lathe. A new cutting edge was used for every cutting speed. The feed rate and depth of cut were kept constant at 0.1 mm/rev and 2.5 mm respectively. The length of cut was limited to 5 mm in order to minimize variability introduced by tool wear. The process parameters, as summarized in Table 1, were selected as appropriate to the cutting tests in the HSM range.

2.2 Temperature measurement

Various experimental techniques have been developed and utilized to study cutting temperatures. Boothroyd [25] in an early work used a photographic technique to study the temperature distribution.

Wanigarathne *et al.* [26] used an infrared (IR) imaging system to measure transient temperature at different points (spots) on the cutting tool during orthogonal machining of AISI 1045 steel with coated grooved tools. An inverse method, together with infrared temperature measurements, was applied by Kwon *et al.* [27] to calculate the temperatures at the tool–chip interface. Davies *et al.* [28] used the finite element method in modelling the cutting tool temperature field and correlating it with the experimental infrared measurements of the temperature fields at the tool–chip interface during orthogonal machining of AISI 1045 steel.

M'Saoubi *et al.* [29] used an IR thermo-video camera to measure temperatures in the deformation zone ahead of the cutting tool tip. M'Saoubi and Chandrasekaran [30] successfully used an IR imaging technique based on charge-coupled device (CCD) sensors to determine temperature distributions in the orthogonal turning of SS2541 (SAE 4337) steel with uncoated (grade P20 S6) and TiN-coated tools. The authors concluded that PVD TiN coatings decreased by 30–35 °C the maximum rake temperatures as observed using the IR-CCD based imaging technique. The size of the heat source was reduced, as a smaller tool–chip plastic contact length was observed when machining with the coated tool, resulting in less heat propagation into the cutting tool. Davies *et al.* [31] obtained IR thermal images from machining experiments with tungsten carbide tools and compared the temperature distributions with those obtained from a finite element analysis. Recently, Davies *et al.* [32] reviewed several temperature measurement methods and described how they can be applied to temperature monitoring during material removal. They detailed the sources of uncertainty in measuring/evaluating temperature using these techniques. Filice *et al.* [33] obtained IR thermal images from turning experiments with uncoated carbide tools and compared the temperature

Table 1 Summary of experimental conditions

Machine tool	Dean Smith & Grace lathe machine (1910T lathe), UK
Workpiece material	AISI/SAE 4140
Workpiece size	200 mm external diameter and 2.5 mm tube thickness
Cutting inserts	TCMW 16T304 5015 (uncoated carbide tool) TCMW 16T304 6620 (TiN-coated tool)
Tool holder	STGCR/L 2020K 16
Cutting velocity, V_c	100, 197, 314, 395, 565, 628, 785, and 880 m/min
Feedrate, f	0.1 mm/rev
Depth of cut, a_p	2.5 mm
Environment	Dry orthogonal machining

Table 2 Thermographic system technical specifications

IR detector	Quantum well IR photodetector (QWIP)
Spectral range	8–9 μm
Image frequency	50/60 Hz non-interlaced (standard), up to 750/900 Hz (optional and with Researcher HS option)
Thermal sensitivity	20 mK at 30 °C
Temperature range	−20 to +2000 °C
Accuracy	± 1% or ± 1 °C (for measurement ranges up to +150 °C) ± 2% or ± 2 °C (for measurement ranges above +150 °C)
Spatial resolution	1.1 mrad
Pixel per image	320 × 240
Zoom function	4 ×
File format	14-bit radiometric IR digital image (IMG) 8-bit standard bitmap (BMP)

distributions with those obtained numerically. Thus, it appears from the literature that IR thermal imaging is a useful technique for obtaining temperature distributions in cutting.

In the present work, temperatures are measured using an IR thermal imager FLIR ThermaCAM® SC3000, a long-wave and self-cooling analysis system with a cool-down time of < 6 min. It has a temperature range of −20 to +2000 °C with an accuracy of ± 2 per cent or ± 2 °C for measurement ranges above 150 °C. This camera can capture and store thermal images and data at high rates of up to 750 Hz PAL/900 Hz NTSC with the ThermaCAM ResearcherTM HS package. Complete technical specifications of the utilized thermal imaging system are given in Table 2. This package allows extensive analysis of highly dynamic objects and events typically found in metal machining research applications. The IR thermal imager FLIR ThermaCAM SC3000 was mounted near the machine turret and placed directly over the tool rake face during cutting tests. The cutting tool temperatures were measured at three different points (spots P_1 to P_3) on the tool rake face, as shown in Fig. 3. These three spots were appropriately selected as prominent observable locations on the rake face of the cutting tool. A high-resolution thermal imaging system was utilized, making it possible to generate thermal maps of the cutting tool insert rake face at distances away from the chip flow zone for the points (spots P_1 to P_3) in order to observe the thermal images clearly and avoid the effect of chip obstruction during machining, as shown in Fig. 4.

The ThermaCAM SC3000 was set up and the location of the analysis area was chosen to be on the cutting tool insert. The camera was positioned at a distance of 25 cm from the insert in order to avoid any damage by the chips. The stored images were recalled and analysed by using available software. When placed on the image, the spotmeter gave the temperature value at the required points (spots P_1 to P_3).

The real temperature of an object depends strongly on the emissivity of the material, which is of particular concern when a thermal imaging camera is used. An
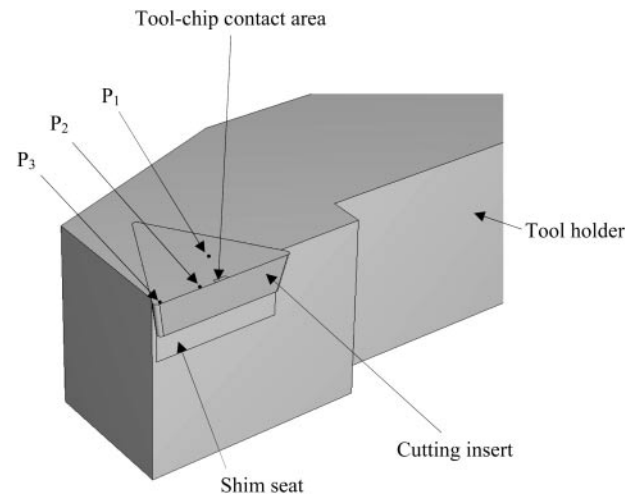

Fig. 3 Insert and tool holder system

accurate calibration of the thermographic system was carried out to find the emissivity values of the cutting tool materials (uncoated and TiN-coated inserts). Samples were heated to temperatures ranging from 100 to 900 °C in an oven. A thermal imaging camera was used to read the temperature of the inserts, and the emissivity was adjusted until the temperature reading of the thermal imager matched a thermocouple reading. The average thermal emissivities of the uncoated cemented carbide and TiN-coated tool inserts were determined to be 0.48 and 0.21 respectively at 700 °C.

3 FINITE ELEMENT MODELLING OF THE HEAT TRANSFER PROCESS

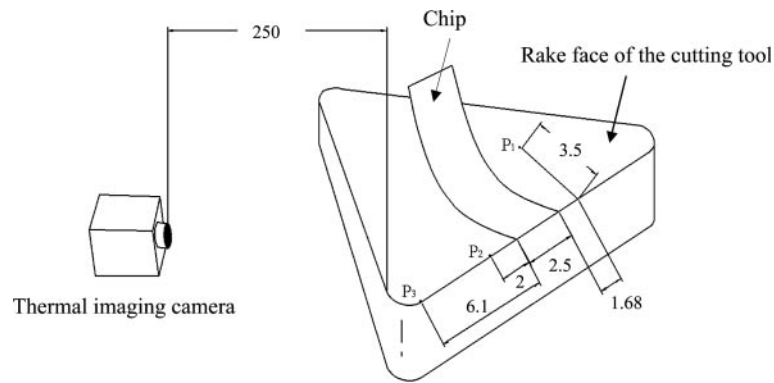A commercial finite element software ABAQUS/Standard (6.5-4) was used to solve the transient

Fig. 4 Schematic thermographic measurement of the specified points (spots P_1 to P_3) (all dimensions are in mm)

Table 3 Summary of mechanical and thermal properties of the cutting tools and the tool holder materials [**23**, **34–38**]

Properties of uncoated cemented carbide cutting tool									
Young's modulus (GPa)	534								
Poisson's ratio	0.22								
Density (kg/m^3)	11 900								
Thermal conductivity (W/m °C)	40.15	44.35	48.55	52.75	56.95	61.15	65.35	69.55	73.75	77.95
at temperature (°C)	100	200	300	400	500	600	700	800	900	1000
Specific heat capacity (J/kg °C)	346.01	358.01	370.01	382.01	394.01	406.01	418.01	430.01	442.01	454.01
at temperature (°C)	100	200	300	400	500	600	700	800	900	1000
Properties of TiN-coated cutting tool									
Young's modulus (GPa)	250								
Poisson's ratio	0.25								
Density (kg/m^3)	5420								
Thermal conductivity (W/m °C)	21	21.47	22	22.52	23.0	23.72	24.38	25.01	25.5	26
at temperature (°C)	100	200	300	400	500	600	700	800	900	1000
Specific heat capacity (J/kg °C)	702.60	752.70	783.40	801.16	818.9	833.46	846.39	856	857.6	859.31
at temperature (°C)	100	200	300	400	500	600	700	800	900	1000
Properties of tool holder (AISI 1045)									
Young's modulus (GPa)	207								
Poisson's ratio	0.3								
Density (kg/m^3)	7844								
Thermal conductivity (W/m °C)	50.70	48.20	45.30	41.90	38.10	33.90	30.10	24.70	25.75	26.80
at temperature (°C)	100	200	300	400	500	600	700	800	900	1000
Specific heat capacity (J/kg °C)	470.40	520.80	571.20	621.60	672.00	722.40	772.80	823.20	873.60	924
at temperature (°C)	100	200	300	400	500	600	700	800	900	1000

heat transfer problem and simulate heat transfer into the cutting tool insert. The element used to model the whole cutting assembly was a four-node tetrahedral heat transfer element DC3D4. The tool was modelled as a perfectly rigid body because tool materials have significantly high elastic moduli. The analysis was based on the estimated realistic uniform and non-uniform heat flux, where appropriate, applied over the experimentally evaluated tool–chip contact area on the rake face of the cutting insert.

The heat transfer taking place in the tool–chip–work system under transient heat conduction in three dimensions is governed by the partial differential equation as

$$\frac{\partial^2 \theta}{\partial x^2} + \frac{\partial^2 \theta}{\partial y^2} + \frac{\partial^2 \theta}{\partial z^2} + \frac{q_{\mathrm{fr}}(x,y,z,t)}{\lambda_{\mathrm{T}}} = \frac{1}{\alpha_{\mathrm{T}}} \frac{\partial \theta}{\partial t} \qquad (5)$$

where α_{T} and λ_{T} are respectively thermal diffusivity and thermal conductivity values for the tool, and θ is the temperature. During the cutting process, some heat penetrates into the shim seat, the clamping parts, and the holder, and the computational domain cannot be considered as the cutting insert only. Therefore, models were developed for both an
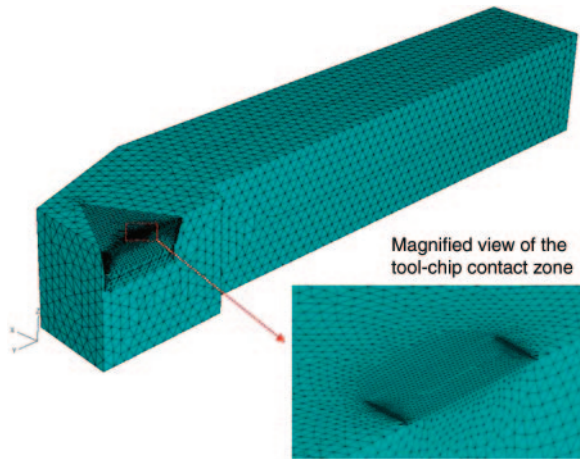
Fig. 5 Finite element mesh for the assembly tool, shim and tool holder in ABAQUS

uncoated cemented carbide insert and a TiN-coated (with 4 μm coating thickness) insert, which consisted of the shim seat, the tool holder, and the clamp screw. Small details of the clamping screw parts were neglected in the models owing to modelling limitations of the analysis package. The thermal properties of the materials used in the model are given in Table 3. Figure 5 shows the finite element mesh, with refinement of the mesh near the cutting edge. The final meshes consisted of 109 903 and 130 451 tetrahedral elements for uncoated and TiN inserts respectively.

The frictional heat at the tool rake face results in a temperature rise for the cutting tool. To calculate the fraction of this heat entering the tool, 100 per cent heat intensity was applied initially on the identified contact area as heat input to the model. This percentage was then reduced until the measured and simulated temperatures were matched at points P_1, P_2, and P_3.

For the heat transfer calculation, the following boundary conditions were used.

1. The cutting insert, shim seat, and tool holder interaction surfaces were assumed to be smooth and held together with a rigid clamping system and were assumed to be in perfect contact.
2. Initially the whole model was set at room temperature ($\theta_0 = 25\,^\circ$C).
3. For non-interactive surfaces of the cutting insert, shim seat, and workpiece, heat losses due to heat convection were calculated using a convective heat transfer coefficient $h = 20$ W/m$^2\,^\circ$C [37].
4. The furthest end-surface of the tool holder, which is distant from the cutting zone, was assumed to be at room temperature.

4 RESULTS AND DISCUSSION

4.1 Cutting forces

Figure 6 shows the variation in cutting forces with cutting speed. The cutting force decreases when the cutting speed is increased from 100 to 395 m/min, marginally increases with the cutting speed up to 565 m/min, and subsequently decreases in the high-speed cutting region. On the other hand, for TiN-coated tools, cutting forces gradually decrease when the cutting speed is increased from 100 to 880 m/min. The experimentally measured cutting and feed force values for the uncoated cemented carbide tools are higher than those of the TiN-coated tools for the whole range of cutting speeds. This trend could be due to the TiN-coating which reduces friction and adhesion with the workpiece. The feed force also decreases gradually when the cutting speed is increased in all the cutting tests for both uncoated cemented carbide and TiN-coated tools.

4.2 Tool–chip contact area

The nature of contact between the chip and tool rake face has a major influence on the mechanics of machining, heat generation, and heat partition into the cutting tool. In this study, the tool–chip contact areas of the worn uncoated cemented carbide and TiN-coated inserts were obtained at different cutting speeds from a Polyvar optical microscope equipped with image-processing software. Sample optical images of the worn insert are shown in Fig. 7. Figure 8 presents the calculated tool–chip contact area obtained from the optical microscope images of the worn inserts at different cutting speeds for uncoated and TiN-coated tools. It is observed that the contact area is significantly affected by the cutting speed. For uncoated tools there is a decrease in the contact area when the cutting speed is increased from 100 to 395 m/min. Beyond 395 m/min, the contact area increases with the cutting speed. This trend is in agreement with the widely reported reduction in contact area for lower cutting speeds and also agrees with more recent findings [23] in the high-speed machining region. On the other hand, with TiN-coated tools, the contact area decreases with increasing cutting speed in both conventional and HSM regions. These results clearly show that TiN coatings mitigate the expansion of the contact area at higher cutting speeds.

4.3 Determination of sticking and sliding regions

As mentioned earlier, at any instant during the cutting process, a part of the interface can be in seizure while the rest of the contact undergoes interfacial
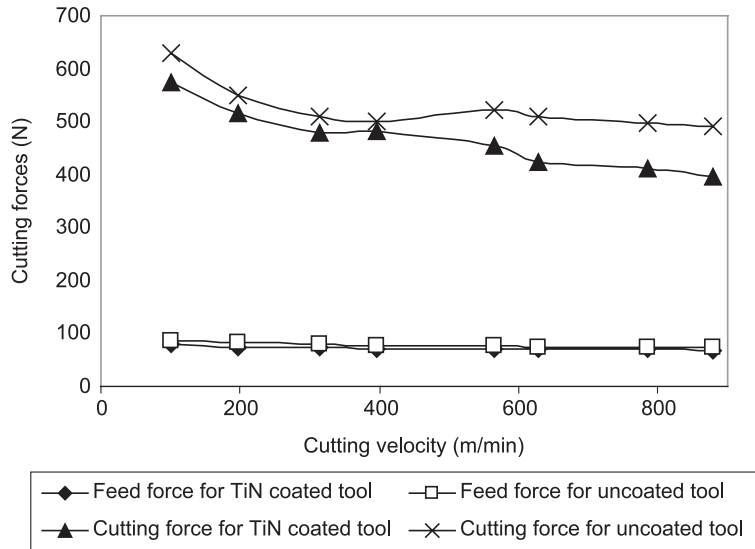
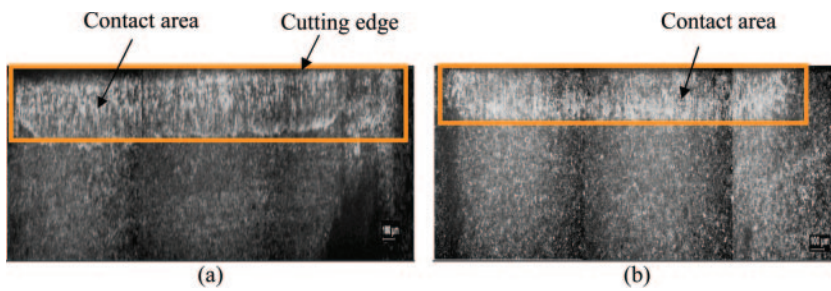**Fig. 6** Variation in cutting forces with cutting speed

Fig. 7 Optical microscope images of the rake face at a cutting speed of 880 m/min for (a) uncoated carbide insert and (b) TiN-coated inserts
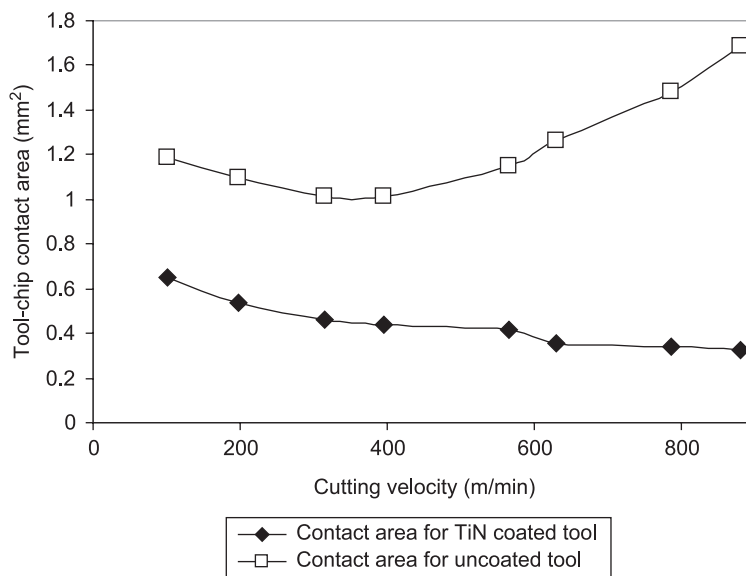

Fig. 8 Variation in tool–chip contact area with cutting speed

sliding. These interfacial conditions are highly dependent on the cutting conditions and the properties of the tool and the workpiece materials [8, 39]. In this work, scanning electron microscopy (SEM) and energy-dispersive X-ray analysis (EDXA) were used to distinguish between the sticking and the sliding regions from an examination of the tool–chip contact region for both uncoated and TiN-coated tools. The worn inserts were examined by SEM using a backscattered imaging mode for the range of cutting speeds. The contact length was scanned for evidence of iron (Fe) transfer from the chip. The evaluation of this Fe transfer intensity was taken on a cross-sectional plane of the contact area in the direction of chip flow.

Figures 9(a) to (f) show the EDXA of Fe concentration maps of the rake face of the cutting inserts for the uncoated and TiN-coated tools for cutting speeds ranging from 100 to 880 m/min. All the micrographs show a low concentration of Fe about the cutting edge, and this is attributed to the effect of the tool edge radius. Figure 9(a) shows that at 100 m/min the tool rake face is not dominated by Fe transfer from the chip, hence providing evidence that seizure does not occur at this cutting speed. As the cutting speed is increased to 565 m/min (Fig. 9(b)), the nature of the contact changes and the tool rake face is dominated by a significant amount of Fe transfer, thereby suggesting the tribological phenomenon of seizure taking place. For a higher cutting speed of 880 m/min there are high peaks of Fe near the edge of the rake face within the contact length (Fig. 9(c)). Fe peaks support a dominant sticking condition. For uncoated carbide cutting tools, it is justifiable to conclude from Figs 9(a) to (c) that no significant sticking or seizure occurred for 100 m/min, with 85 per cent sticking and 15 per cent sliding at 565 m/min, and 100 per cent sticking at 880 m/min.

For TiN-coated tools, at a low cutting speed 100 m/min, no significant concentration of Fe is present (less than 10 per cent), indicating the absence of material transfer or sticking and hence supporting a dominant sliding condition (Fig. 9(d)). When the cutting speed increases to 565 m/min, still no dominant Fe concentration is present (Fig. 9(e)), again supporting a prevalent sliding condition. At the highest cutting speed of 880 m/min (Fig. 9(f)), about 32 per cent of the contact area shows significant Fe transfer, and hence a 32 per cent sticking (seizure) and 68 per cent sliding are established for this case.

4.4 Heat partition into the cutting tool

Figure 10 shows typical simulation results for the temperature distribution at the cutting insert for a non-uniform heat input at a cutting speed of 565 m/min for uncoated and TiN-coated tools. These distributions clearly show the presence of high temperature gradients near the cutting edge. The relatively high temperatures are expected owing to the high strength of the machined workpiece alloy and high depth of cut which was set at 2.5 mm.

In the estimation of heat partition into the cutting tool with the combined FEM–experimental approach, a slight disagreement was observed between 'single-point' and 'multiple-point' temperature matching for both uncoated and TiN-coated tools. Errors in the prediction of heat partition owing to temperature matched at a single point (P_1) and multiple points (P_1, P_2, and P_3), range from -14.0 to $+1$ per cent considering results for both types of cutting tool. This variation could be due to the fact that, when one point is selected for temperature matching, the thermal plane is not constrained. It is also plausible that non-uniform heat intensity can exist in the depth-of-cut direction, for example driven by chip curl. However, the low percentage variation between the single-point and multiple-point matching cases shows that single-point matching can still provide a reasonable computational basis for predicting heat flux.

Figure 11 compares heat partition into the cutting tool for uncoated and TiN-coated tools following the combined FEM–experimental approach and multiple-point matching. In the conventional cutting speed range of 100–395 m/min, the heat partition coefficient obtained for uncoated cemented carbide tools varies from 41 down to 17 per cent. For TiN-coated tools the heat partition varies from 35 down to 16.7 per cent. These ranges are representative of the values discussed earlier [20–23] for conventional machining, thus further validating the integrity of the combined FEM–experimental approach employed in this study. A continuously decreasing trend for heat partition into the cutting tool is observed with TiN-coated tools for the whole range of cutting speeds, as supported by the contact area which reduces with increasing cutting speeds (Fig. 8).

In addition [40], thermal effects caused by coatings have an important influence on the tribological behaviour between the cutting tool and the chip. The amount of thermal energy transferred into the chip body depends on the thermal conductivity of the coating film deposited on the cutting tool insert. When the thermal conductivity of the cutting tool is low, then the temperature in the chip will be high, and consequently the fraction of heat entering the cutting tool will be low. Furthermore, there is a direct correlation between the tool–chip contact length, the properties of the cutting tool, and the performance of the cutting process. For this reason, cutting tool materials with low thermal conductivity produce more curled chips because of a thermal bimetallic effect. As presented earlier, Table 3 shows the temperature-dependent thermal conductivity values
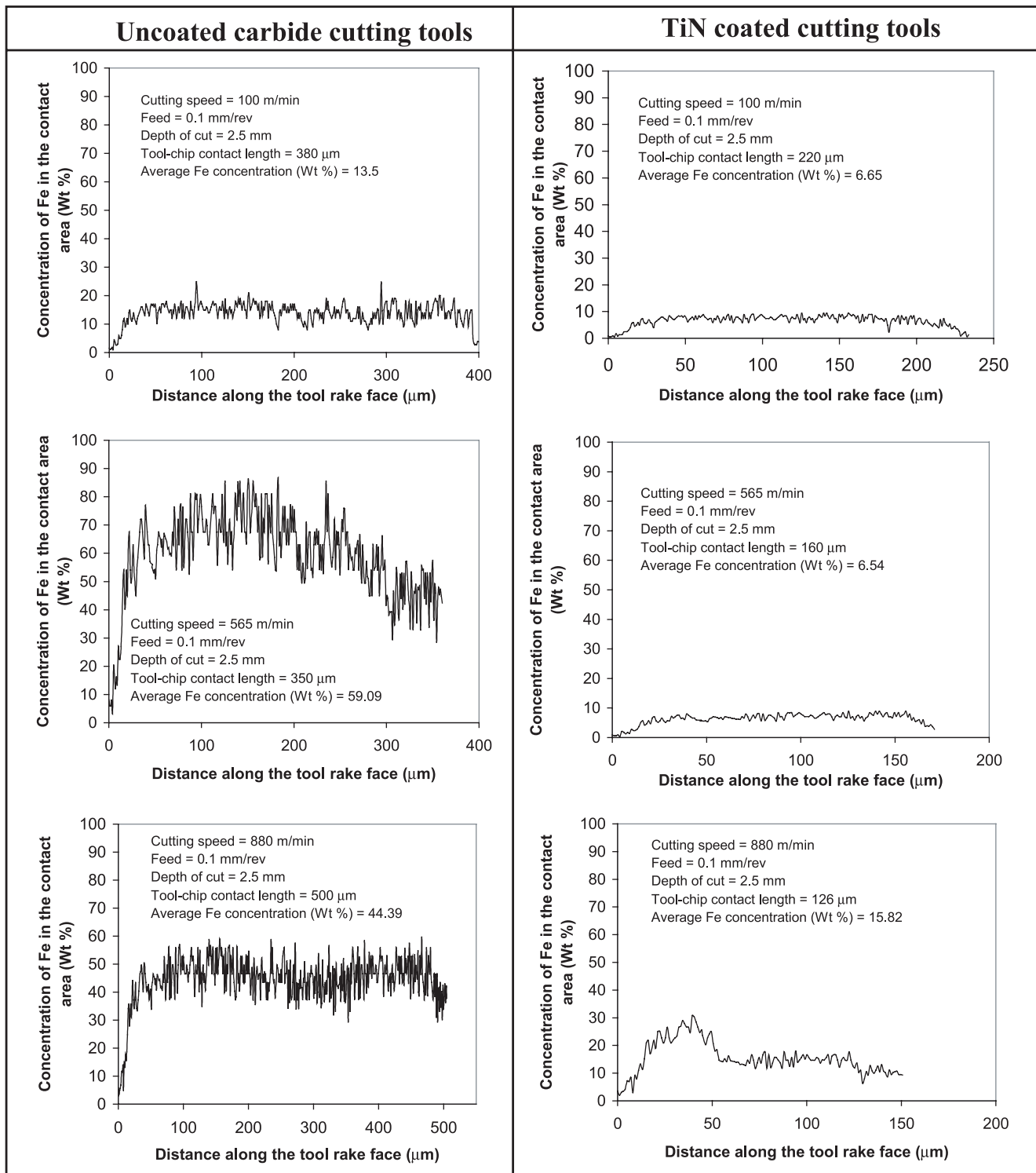
Fig. 9 SEM-EDXA Fe density maps along the rake face of uncoated carbide and TiN-coated cutting inserts for cutting speeds of 100 m/min (a, d), 565 m/min (b, e) and 880 m/min (c, f)

for uncoated cemented carbide and TiN cutting tool materials. It can be seen in this table that the thermal conductivity values of the TiN coating are lower than those of the uncoated tools.

Figure 11 shows, for both uncoated and TiN-coated tools, a reduction in the value of heat partition into the cutting tools obtained from the combined FEM–experimental approach with an increase in the
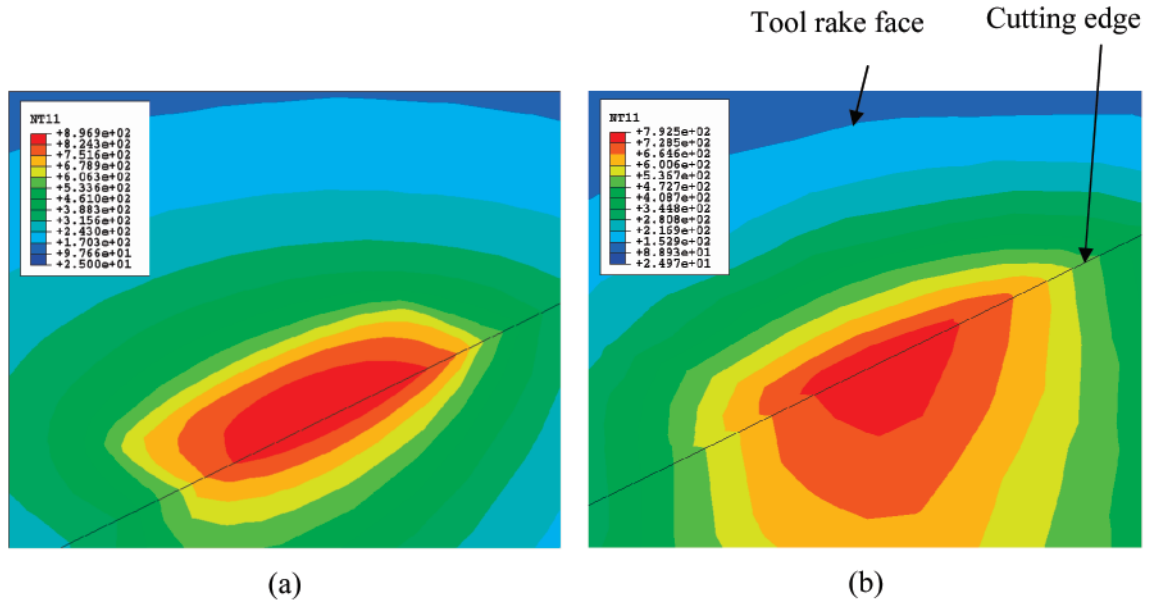
Fig. 10 Temperature distribution results at a cutting speed of 565 m/min for (a) an uncoated cemented carbide tool and (b) a TiN-coated tool
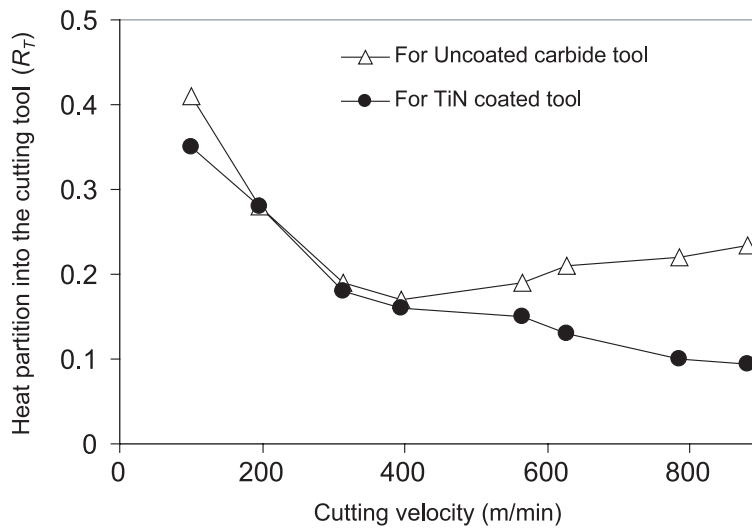

Fig. 11 Variation in heat partition with cutting speed

cutting speed from 100 to 395 m/min, i.e. within the conventional and the transition cutting speed regions. These trends at lower cutting speeds are influenced by the well-known reduction in the contact length and hence the contact area (Fig. 8). When the cutting speed is increased above 395 m/min in the HSM region, the nature of the contact changes and the tool–chip contact length, and hence the contact area, increases for uncoated tools. As a consequence, Fig. 11 shows that the fraction of heat flowing into the uncoated tool gradually increases with the cutting speed and reaches 23.5 per cent at 880 m/min. In contrast, above 395 m/min, the

tool–chip contact length, and hence the contact area, decreases for TiN-coated tools. For this case, Fig. 11 shows that the fraction of heat flowing into the TiN-coated tool gradually decreases with the cutting speed and reaches 9.5 per cent at 880 m/min. This implies that the use of single-layer TiN-coated tools compared with the uncoated tools can cause a reduction in heat partition into the cutting tool by about 17 per cent at conventional cutting speeds and 60 per cent in the HSM region. The benefits of reduction in heat partition brought by the TiN coating are more pronounced in HSM compared with conventional machining.

5 CONCLUSIONS

1. A combined FEM–experimental approach is employed for accurate estimation of the fraction of heat going into the cutting tool for conventional and high-speed machining with uncoated and TiN-coated tools. This approach is based on simultaneously matching the measured and simulated temperatures at multiple points. The approach is validated with the published numerical heat partition values for uncoated tools in conventional machining.

2. The numerical model used here applies non-uniform heat intensity, where appropriate, based on a quantitative determination of sticking and sliding zones at the tool–chip interface which are established from EDXA material transfer analysis.

3. From the energy-dispersive X-ray line scanning measurements, the effects of cutting speed on the sticking and sliding lengths have been determined on the basis of the Fe transfer maps. While sliding friction is common in conventional machining, in HSM seizure takes place for uncoated carbide tools. The use of the TiN coating alleviates contact area expansion, as well as the transfer of Fe from the chip.

4. It is found that the use of TiN-coated tools causes a reduction in heat partition into the cutting tool compared with the uncoated tool: about 17 per cent at conventional cutting speeds, and 60 per cent in the HSM region.

5. It may be concluded that, compared with uncoated carbide tools, TiN coatings significantly improve the tribological phenomena by reducing the tool–chip contact area, providing a lower thermal conductivity for the tooling systems, and ultimately reducing heat partition into the cutting tool.

REFERENCES

1 **Fallbohmer, P., Rodriguez, C. A., Ozel, T.,** and **Altan, T.** High-speed machining of cast iron and alloy steels for die and mold manufacturing. *J. Mater. Processing Technol.*, 2000, **98**, 104–115.

2 **Schulz, H.** and **Moriwaki, T.** High-speed machining. *Ann. CIRP*, 1992, **41**(2), 637–643.

3 **König, W.** New approaches to characterize cutting tool coatings. *Ann. CIRP*, 1992, **41**(1), 49–52.

4 **Rech, J.** and **Djouadi, M. A.** High speed gear hobbing. *Wear*, 2001, **250**, 45–53.

5 **Erdemir, A.** and **Hochman, R. F.** Surface metallurgical and tribological characteristics of TiN-coated bearing steels. *Surf. Coatings and Technol.*, 1988, **36**, 755–763.

6 **Wallen, P.** and **Hogmark, S.** Influence of TiN coating on wear of high speed steel at elevated temperature. *Wear*, 1989, **130**, 123–135.

7 **Trent, E. M.** *Metal cutting*, 2nd edition, 1984 (Butterworth & Co, London, UK).

8 **Trent, E. M.** Metal cutting and the tribology of seizure, i: Seizure in metal cutting. *Wear*, 1988, **128**, 29–45.

9 **Trent, E. M.** Metal cutting and the tribology of seizure, ii: Movement of work material over the tool in metal cutting. *Wear*, 1988, **128**, 46–64.

10 **Blok, H.** Theoretical study of temperature rise at surfaces of actual contact under oiliness lubricating conditions. In Proceedings of General Discussion on *Lubrication and Lubricants*, Institute of Mechanical Engineers, London, UK, 1938, pp. 222–235.

11 **Chao, B. T.** and **Trigger, K. J.** Temperature distribution at the tool–chip interface in metal cutting. *Trans. ASME*, 1955, **72**, 1107–1121.

12 **Chao, B. T.** and **Trigger, K. J.** Temperature distribution at tool–chip and tool–work interface in metal cutting. *Trans. ASME*, 1958, **80**(1), 311–320.

13 **Komanduri, R.** and **Hou, Z. B.** Thermal modeling of the metal cutting process, part ii: Temperature rise distribution due to frictional heat source at the tool–chip interface. *Int. J. Mech. Sci.*, 2001, **43**, 57–88.

14 **Huang, Y.** and **Liang, S. Y.** Cutting temperature modeling based on non-uniform heat intensity and partition ratio. *Mach. Sci. and Technol.*, 2005, **9**, 301–323.

15 **Karpat, Y.** and **Özel, T.** Predictive analytical and thermal modeling of orthogonal cutting process – part i: Predictions of tool forces, stresses, and temperature distributions. *Trans. ASME, J. Mfg Sci. and Engng*, 2006, **128**, 435–444.

16 **Karpat, Y.** and **Özel, T.** Predictive analytical and thermal modeling of orthogonal cutting process – part ii: Effect of tool flank wear on tool forces, stresses, and temperature distributions. *Trans. ASME, J. Mfg Sci. and Engng*, 2006, **128**, 445–453.

17 **Moriwaki, T., Sugimura, N.,** and **Luan, S.** Combined stress, material flow and heat analysis of orthogonal machining of copper. *Ann. CIRP*, 1993, **42**(1), 75–78.

18 **Takeuchi, Y., Sakamoto, M.,** and **Sata, T.** Improvement in the working accuracy of an nc lathe by compensating for thermal expansion. *Precision Engng*, 1982, **4**(1), 19–24.

19 **Wright, P. K., McCormick, S. P.,** and **Miller, T. R.** Effect of rake face design on cutting tool temperature distributions. *Trans. ASME J. Engng for Industry*, 1980, **102**(2), 123–128.

20 **Lo Casto, S., Lo Valvo, E.,** and **Micari, F.** Measurement of temperature distribution within tool in metal cutting. Experimental tests and numerical analysis. *J. Mech. Working Technol.*, 1989, **20**, 35–46.

21 **Grzesik, W.** and **Nieslony, P.** A computational approach to evaluate temperature and heat partition in machining with multilayer coated tools. *Int. J. Mach. Tools and Mf*, 2003, **43**, 1311–1317.

22 **Loewen, E. G.** and **Shaw, M. C.** On the analysis of cutting tool temperatures. *Trans. ASME*, 1954, **71**, 217–231.

23 **Abukhshim, N. A., Mativenga, P. T.,** and **Sheikh, M. A.** Investigation of heat partition in high speed turning of high strength alloy steel. *Int. J Mach. Tools and Mf*, 2005, **45**, 1687–1695.

24 **Tay, A. E., Stevenson, M. G.,** and **DeVahl Davis, G.** Using the finite element method to determine

temperature distribution in orthogonal machining. *Proc. Instn. Mech. Engrs*, 1974, **188**, 627–638.

25 **Boothroyd, G.** Temperatures in orthogonal metal cutting. *Proc. Instn. Mech. Engrs*, 1963, **177**(29), 789–810.

26 **Wanigarathne, P. C., Kardekar, A. S., Dillon, O. W., Poulachon, G.,** and **Jawahir, I. S.** Progressive tool-wear in machining with coated grooved tools and its correlation with cutting temperature. *Wear*, 2005, **259**, 1215–1224.

27 **Kwon, P., Schiemann, T.,** and **Kountanya, R.** An inverse estimation scheme to measure steady-state tool–chip interface temperatures using an infrared camera. *Int. J. Mach. Tools and Mf*, 2001, **41**, 1015–1030.

28 **Davies, M. A., Cao, Q., Cooke, A. L.,** and **Ivester, R.** On the measurement and prediction of the temperature fields in machining. *Ann. CIRP*, 2003, **52**, 77–80.

29 **M'Saoubi, R., Le Calvez, C., Changeux, B.,** and **Lebrun, J. L.** Thermal and microstructural analysis of orthogonal cutting of low alloyed carbon steel using an infrared-charge-coupled device camera technique. *Proc. Instn. Mech. Engrs, Part B: J. Engineering Manufacture*, 2002, **216(B)**, 153–165.

30 **M'Saoubi, R.** and **Chandrasekaran, H.** Investigation of the effects of tool microgeometry and coating on tool temperature during orthogonal turning of quenched and tempered steel. *Int. J. Mach. Tools and Mf*, 2004, **44**, 213–224.

31 **Davies, M. A., Cooke, A. L.,** and **Larsen, E. R.** High bandwidth thermal microscopy of machining AISI 1045 steel. *Ann. CIRP*, 2005, **54**(1), 63–66.

32 **Davies, M. A., Ueda, T., M' Saoubi, R., Mullany, B.,** and **Cooke, A. L.** On the measurement of temperature in material removal processes. *Ann. CIRP*, 2007, **56**(2), 581–604.

33 **Filice, L., Umbrello, D., Beccari, S.,** and **Micari, F.** On the FE codes capability for tool temperature calculation in machining processes. *J. Mater. Processing Technol.*, 2006, **174**, 286–292.

34 **Kim, H.** and **Oh, S. I.** Evaluation of heat transfer coefficient during heat treatment by inverse analysis. *J. Mater. Processing Technol.*, 2001, **112**, 157–165.

35 **Childs, T., Maekawa, K., Obikawa, T.,** and **Yamane, Y.** *Metal machining theory and applications*, 2000 (Arnold, London, UK).

36 **Gale, W. F.** and **Totemeier, T. C.** *Smithells metals reference book*, 2004 (Elsevier, London, UK).

37 **Yen, Y.-C., Jain, A., Chigurupati, P., Wu, W.-T.,** and **Altan, T.** Computer simulation of orthogonal cutting using a tool with multiple coatings. *Mach. Sci. and Technol.*, 2004, **8**(2), 305–326.

38 **Lengauer, W., Binder, S., Aigner, K., Ettmayer, P., Guillou, A., Debuigne, J.,** and **Groboth, G.** Solid state properties of group IVb carbonitrides. *J. Alloys and Compounds*, 1995, **217**, 137–147.

39 **Gekonde, H. O.** and **Subramanian, S. V.** Tribology of tool–chip interface and tool wear mechanisms. *Surf. and Coatings Technol.*, 2002, **149**, 151–160.

40 **Jawahir, I. S.** and **Van Luttervelt, C. A.** Recent developments in chip control research and applications. *Ann. CIRP*, 1993, **42**(2), 659–693.

APPENDIX

Notation

a_p depth of cut (mm)
f feed rate (mm/rev)
F_c cutting force (N)
F_f feed force (N)
F_{fr} frictional force at the rake face (N)
h convective heat transfer coefficient (W/m$^2\,^\circ$C)
l_{ch} tool–chip contact length (mm)
l_{sl} sliding length of the tool–chip contact zone (mm)
l_{st} sticking length of the tool–chip contact zone (mm)
q_{fr} non-uniform heat intensity along the tool–chip interface (W/mm^2)
R_T fraction of the heat conducted into the cutting tool
t undeformed chip thickness (mm)
t_{ch} actual chip thickness (mm)
V_c cutting velocity (m/min or m/s, as defined)
V_{ch} chip velocity (m/s)

α_T thermal diffusivity of the tool material (mm^2/s)
γ rake angle (deg)
θ_0 initial tool and workpiece temperature ($^\circ$C)
λ_h chip compression ratio $= t_{ch}/t$
λ_T thermal conductivity of the tool material (W/m K)
τ_{sh} shear stress (N/mm^2)